Ion dynamics in the magnetic nozzle of a waveguide ECR thruster via laser-induced fluorescence spectroscopy

Alfio Vinci, Marco Inchingolo, Stéphane Mazouffre, Jaume Navarro-Cavallé

Ion dynamics in the magnetic nozzle of a waveguide ECR thruster via laser-induced fluorescence spectroscopy

Alfio E Vinci[1], Marco R Inchingolo[2], Stéphane Mazouffre[1] and Jaume Navarro-Cavallé[2]

[1]Institut de Combustion, Aérothermique, Réactivité et Environnement, Centre National de la Recherche Scientifique, 1C Avenue de la Recherche Scientifique, 45071 Orléans, France
[2]Equipo de Propulsión Espacial y Plasmas, Universidad Carlos III de Madrid Avenida de la Universidad 30, 28911 Leganés, Spain

E-mail: alfio.vinci@cnrs-orleans.fr, minching@pa.uc3m.es, stephane.mazouffre@cnrs-orleans.fr, janavarr@ing.uc3m.es

6 November 2022

Abstract. Xenon ion velocity is mapped in the magnetic nozzle of a circular waveguide electron cyclotron resonance thruster operating at 5.8 GHz by means of laser-induced fluorescence spectroscopy in the near-infrared spectral range. An array of thruster operational parameters are explored to investigate the influence on the acceleration profile and terminal ion velocity. Owing to several mechanisms which broaden the measured spectra, e.g. Paschen-Back/Zeeman effect, inference of the most probable velocity along with the axial kinetic temperature requires full lineshape modeling, especially in the near-field plume and inside the source. Ions are effectively accelerated along the magnetic nozzle, reaching up to $12\,000\,\mathrm{m\,s^{-1}}$ for the lowest neutral pressure tested. A relatively large axial kinetic temperature is observed, typically in the order of 5000 K, which can be attributed to an extended ionization region that overlaps with the acceleration region.

Keywords: magnetic nozzle, laser-induced fluorescence, ECRT, electric propulsion

Submitted to: *J. Phys. D: Appl. Phys.*

1. Introduction

A new class of in-space propulsion based on electrodeless discharges is being researched to extend the mission range typically covered by mature technologies, e.g. gridded ion thrusters and Hall thrusters. These devices embed a magnetic nozzle (MN) to enhance the momentum of the ejected ions and come with the promise of increased durability, simpler satellite integration and a current-free plume, relieving from the need of a neutralizer and allowing the extensive use of alternative propellants [1–3]. However, these devices are still far from the performance levels achieved by classical technologies [4–6].

The Electron Cyclotron Resonance Thruster (ECRT) is of central interest in this thruster class, as it exhibits interesting performance metrics [7]. The working principle of an ECRT relies on the electron cyclotron resonance to efficiently transfer power from an electromagnetic wave (typically in the microwave range) to the electrons, rising their perpendicular temperature. This phenomenon occurs locally at the resonance layer, where the condition $\omega_{ce} = \omega$ is met, with $\omega_{ce} = eB/m_e$, the electron cyclotron angular frequency and ω the frequency of the externally applied electromagnetic wave [8, 9]. The conversion of electron thermal energy into ion kinetic energy is then conveyed by the plasma expansion in the magnetic nozzle [10]. The discharge and acceleration mechanisms thus require the existence of an externally applied magnetic field.

Two different microwave injection designs have been reported in the literature for ECRTs, the coaxial [7,11–13] and the truly electrodeless circular waveguide design [14–18]. In the first case, a central conductor is present in the plasma chamber which can be seen as an extension of the coaxial cable delivering the microwaves from the source to the thruster. This component is subject to strong erosion and heat loads and it is absent in the waveguide version. The way microwave power is coupled to the plasma appears to be a relevant factor for electron heating and consequently ion acceleration. Lower performance levels have been reported for the waveguide configuration [13] for similar operating conditions (input microwave power of 25 W at 2.45 GHz, 1 sccm of Xenon) and thruster dimensions. A better understanding of the reasons behind the performance discrepancy is of great importance since it could lead to improved design strategies. For this purpose, mutual efforts coming from both simulations and experiments are necessary. Thus far, because of the limitations set by intrusive diagnostics, little is known about the ion dynamics and plasma potential distribution inside the discharge chamber region of a waveguide ECRT, the only information coming from non-self-consistent plasma simulations [19]. In addition, although the MN physics is common to other similar devices, ion acceleration profiles along the nozzle have never been reported for a waveguide thruster, being this information of key importance for validating future MN models and plasma simulations. In this context, this work examines the ion dynamics in the plume of a waveguide ECRT via near-infrared laser-induced fluorescence (LIF) spectroscopy. The LIF technique has the advantage of being weakly intrusive and capable of high spatial resolution when compared to electrostatic diagnostics, allowing to probe regions otherwise inaccessible without affecting the expansion itself. However, in MN-based discharges, the relatively intense external magnetic field can hinder the easy inference of the ion velocity from the shift of the line center. This is particularly true inside the source and in the proximity of the exit plane, where the field might lead to visible Zeeman and Paschen-Back effects. An accurate estimation of the Doppler shift in this region requires a full modelling of the fluorescence profile by accounting for all broadening mechanisms. As a further result of the lineshape modelling, the axial ion kinetic temperature can be also inferred from a fit of the LIF profiles, offering insights on the ionization-acceleration region in the discharge chamber.

The rest of this study is organized as follows: the experimental arrangement is detailed in Section 2; after commenting on the recorded spectra and discussing the procedure to infer the velocity profiles through lineshape modeling, the results are presented in Section 3; ultimately, conclusions are drawn in Section 4.

2. Experimental arrangement

2.1. Thruster unit and test facility

Figure 1 shows a schematic view of the experimental arrangement in the vacuum chamber facility at the University of Carlos III de Madrid (UC3M). The thruster unit is shown at the top and a detailed description is available in [20, 21]. It mainly comprises a circular waveguide constituting the plasma chamber (PC) and a magnetic field generator. The latter, is made up by two separate components: a permanent magnet (PM) and an electromagnet. The PM consists of a radially magnetized ring, which is made of twelve Sm-Co YXG-32 magnets glued together and enclosed in an aluminium box. The brown solid line in Figure 2(a) depicts the magnetic field strength produced by the PM along the thruster axis. On the other hand, the electromagnet can be used to adapt the shape of the MN and displace the resonance position. The effects of the electromagnet on the magnetic field strength and divergence are shown in figures 2(a)-(b) and 3.

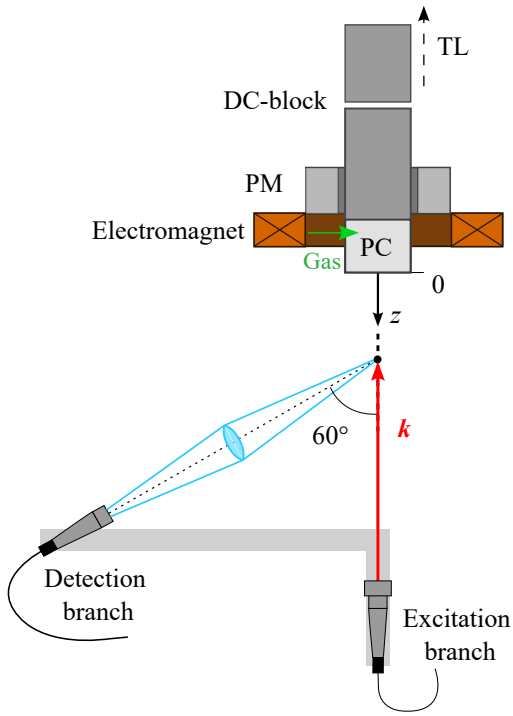

Figure 1. Schematic top view of the experimental setup. The thruster unit (top) and optical arrangement (bottom) are shown. Drawing not in scale.

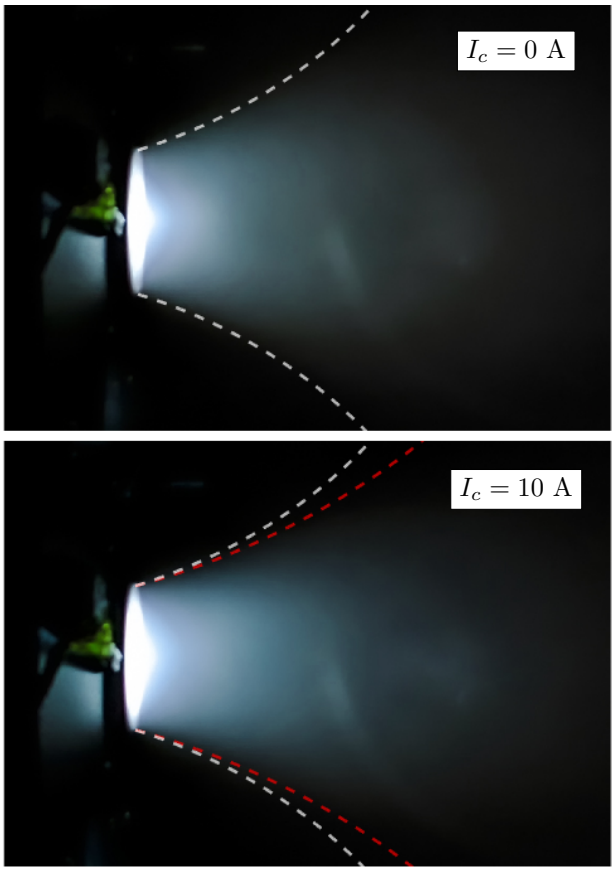

Figure 3. Photographs of the thruster in operation with two different magnetic nozzle shapes. The magnetic streamlines passing from the walls at the exit plane are shown with dashed lines, white for $I_c = 0$ A, red for $I_c = 10$ A.

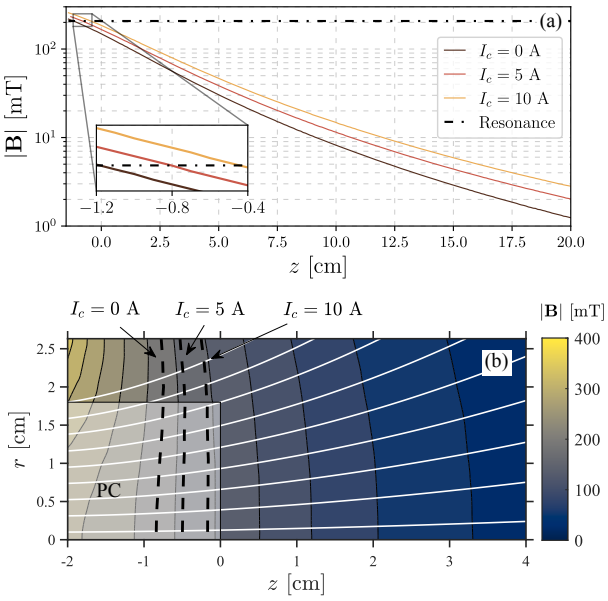

Figure 2. (a) Measured axial profiles of the ECRT magnetic field amplitude, (b) simulated 2-D maps of the MN highlighting the ECR surface as a function of I_c. $z = 0$ refers to the exit plane of the discharge tube. The dash-dotted line indicates the resonance at 5.8 GHz.

The microwave frequency used is 5.8 GHz, allowing for smaller waveguide dimensions than the usual 2.45 GHz frequency, and consequently lowering the size of the device, its mass flow rate and power requirements. A higher frequency comes with the need of a stronger field for reaching the resonance condition ($B_{res} = 0.207$ T at 5.8 GHz). The field generated by the PM alone suffices the ECR condition inside the PC.

The PC is made of stainless steel. Its diameter and length are $D_T = 36$ mm and $L_T = 20$ mm. The PC is separated from the aluminium circular waveguide at the back by a quartz window sealed with a FFKM o-ring. Xenon gas is injected radially in the PC from twelve, 1 mm diameter holes located at $z = -18$ mm on the lateral PC walls.

Microwave power is delivered from the source to the thruster through a waveguide transmission line (TL). More information on the TL used for this work can be found in reference [20] and [21]. The thruster waveguide and consequently the PC is electrically floating with respect to the rest of the TL. This is made possible by a vacuum-gap DC-block consisting

Table 1. Xe II probed optical transition.

	Transition	Wavelength (air)
Xe II	$5d\ ^2[4]_{7/2} \rightarrow 6p\ ^2[3]^\circ_{5/2}$	834.724 nm
	$6p\ ^2[3]^\circ_{5/2} \rightarrow 6s\ ^2[2]_{3/2}$	541.915 nm

of two waveguides aligned and separated by a distance of 2 mm. Negligible power (< 2 %) is lost if the gap is smaller than 3 mm. The thruster floating potential V_T was measured during the overall test campaign. Using the same nomenclature as in [21] the power associated to each of the spectra shown in the following sections is the forward power P_F measured with a directional coupler. P_F differs from the actual power delivered to the thruster, since some power is reflected back to the generator and some is absorbed in the transmission line. As well as P_F, the reflected power is measured with a directional coupler, whereas the transmission line power absorption has been characterized with a Vector Network Analyzer. In general, the power coupled to the plasma is estimated to be between $15 - 20$ % lower of P_F for the tested operating point. A change in the operating conditions i.e. input power, mass flow rate or electromagnet current, can affect the amount of reflected power. A waveguide stub tuner has been used to keep its value always below 5 % of P_F.

The vacuum chamber where experiments are performed consists of a non-magnetic stainless-steel vessel of 1.5 m inner diameter and 3.5 m long. The facility background pressure is about 10^{-7} mbar, whereas the operating pressure remains in the order of 10^{-6} mbar. The vacuum technology implemented in the chamber consists of three cryopanels (COOLPOWER 140 T-V cryoheads by Leybold) and a couple of turbomolelucar pumps, MAG2.200iP by Leybold.

Referring to Figure 1, LIF optics are positioned in front of the thruster and mounted on a linear translation stage. The complete description of the optical diagnostics is available in Section 2.2.

2.2. Optical setup

LIF spectroscopy allows determining the dynamics of atoms and ions. In previous works [22–24], the measurement technique was described in details along with a description of the optical bench used in this study. The probed species is excited using a laser beam produced by an amplified tunable single-mode laser diode in the near-infrared spectral range. The diode can deliver up to 600 mW in the $810 - 840$ nm wavelength range. In the present experiment, the laser remains mod-hop free over a frequency tuning range of about 5 GHz. By splitting the primary laser beam into multiple beams, it is possible to: *i*) monitor continuously the laser mode and detect any mode hop by means of a Fabry-Pérot interferometer; *ii*) accurately measure the laser wavelength by way of a calibrated wavemeter whose absolute accuracy is 80 MHz ($\approx 60\,\mathrm{m\,s^{-1}}$). Modulation of the laser beam power is achieved using a mechanical chopper at ~ 500 Hz.

The laser is coupled to a 50 µm multi-mode optical fiber which transports the beam from the optical bench to the inside of the vacuum facility. Here a custom collimator is employed to shine the laser beam towards the backplate of the ECRT in the direction of the thruster axis z, see Figure 1. At the output of the collimator, the laser beam diameter is about 4 mm, whereas the power density is maintained to $\sim 2\ \mathrm{mW\,mm^{-2}}$, which ensures a weak saturation effect. Note that, in the described configuration, $\mathbf{k} \cdot \mathbf{v} < 0$, where $\mathbf{k}$ is the laser wavevector and $\mathbf{v}$ the ion velocity. The collimator is kept at a safe distance (>20 cm) from the thruster exit plane in order to minimize plume perturbations and avoid overheating and damage of optics. The fluorescence light is collected using a bi-convex lens with 60 mm focal length focusing on a 200 µm core diameter optical fiber. In order to resolve the ion velocity at $z < 0$, the detection branch is tilted by 60 deg with respect to the thruster axis, cf. Figure 1. Both the excitation and detection branches are mechanically linked to a linear translation stage, whose spatial resolution is 1 mm and accuracy ≈ 300 µm. Any relative displacement between the two optical branches is inhibited. This enables points to be probed in the range of $-1\,\mathrm{cm} < z < 20\,\mathrm{cm}$ along the thruster axis. The 200 µm optical fiber transports the fluorescence light to a monochromator which isolates the selected line from the whole spectrum. Afterwards, a photomultiplier tube converts the light signal into voltage, which is fed into a lock-in amplifier operating at the laser modulation frequency to distinguish the signal from the natural plasma emission. A signal deconvolution is not performed in obtaining the lineshapes.

Xenon ions are probed in the $5d\ ^2[4]_{7/2}$ metastable level. The selected optical transition is detailed in Table 1, together with the excitation and fluorescence wavelengths [23, 25–28].

3. Results and discussion

3.1. Observed spectra

Fluorescence spectra are resolved along the thruster axis in a region that extends from $z < 0$ up to several centimeters downstream the exit plane. The farthest distance being probed is limited by the signal-to-noise ratio of the recorded spectra and it depends on

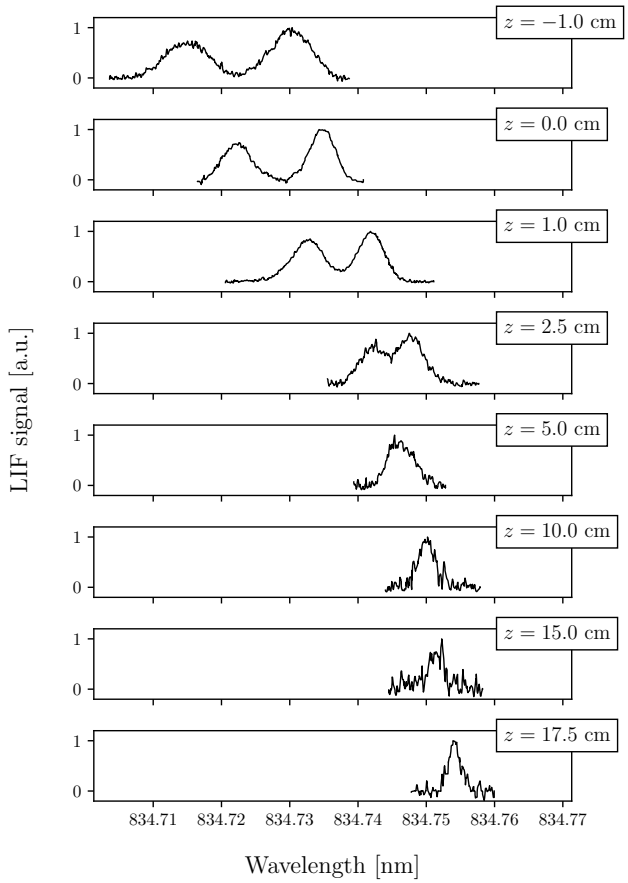

Figure 4. LIF spectra resolved along z. Wavelength values are expressed for air. Thruster operation parameters are: $P_F = 200$ W, $\dot{m} = 2$ sccm, $I_c = 0$ A.

the thruster operating conditions. Signal acquisition has been possible up to $z = 20$ cm at low mass flow rate. Close to the exit plane, the entire fluorescence profile covers a range of about 15 GHz, therefore three separated frequency scans needed to be recorded and merged during post-processing.

A typical series of axial scans is shown in Figure 4. It is observed that the fluorescence profiles feature a double-peak shape in the proximity of $z = 0$. At larger axial distances, the two peaks merge resulting in a broad profile (e.g. at $z = 5$ cm in Figure 4) that eventually reduces to a narrow Gaussian-like spectrum farther downstream. Qualitatively similar results have been observed in a recent experiment performed on a helicon plasma thruster [24]. Starting from the raw lineshapes, the most probable velocity of the probed species is given by the Doppler shift of the line center. However, when the fluorescence light profile does not feature a quasi-Gaussian shape, the shifted line center cannot be easily identified, making it impossible to accurately retrieve the most probable velocity. Following the discussion reported in [24], the raw spectra recorded near $z = 0$ do not image the local ion velocity distribution function (IVDF). The relatively strong magnetic field inside the source and in the near-field plume determines the splitting of the energy levels. This phenomenon leads to a complex lineshape as exemplified in Figure 4. Other LIF studies on ECR thrusters [12, 29] did not observe such a prominent effect on the experimental profiles. This fact has been attributed to the weaker magnetic field within the probed domain [29]. In the current experiment, it is found that departure from a quasi-Gaussian profile occurs at field strengths greater than ~ 30 mT. As a result, modeling of the fluorescence profiles needs to be addressed for the accurate determination of the ion velocity.

It is worth mentioning that the presence of multiple populations ions, e.g. resulting from charge-exchange (CEX) collisions, cannot justify the profiles recorded in this experiment. In fact, this hypothesis would not provide an explanation for the absence of slow ions farther downstream the exit plane.

3.2. Lineshape modeling

The purpose of this section is to provide a broad overview of the theory that has been implemented to reconstruct the fluorescence profiles of interest for this experiment. A more detailed treatment can be found in [24] and the references therein included.

The spectrum is modeled accounting for seven stable xenon isotopes having a natural abundance >1 % [30]. Each isotope leads to the so called isotopic shift due to mass and volume differences in the nucleus, whereas those isotopes with odd atomic number (^{129}Xe and ^{131}Xe) possess a nonzero nuclear spin I and therefore lead to the hyperfine structure (HFS). On top of that, the external magnetic field further splits each spectral line into several components. This effect is accounted for either in the weak or strong field approximation. The former is called Zeeman effect, while the latter corresponds to the Paschen-Back effect. The choice of relying either on the weak or strong field approximation depends on the local strength of the external magnetic field in the context of the hyperfine interaction [31]. In practice, the complete modeling procedure consists in:

(i) finding every allowed optical transition;
(ii) quantifying the associated detuning frequency;
(iii) determining the relative intensity of each line;
(iv) accounting for Doppler broadening and Doppler shift.

First, the upper and lower energy levels of the probed transition are solved by determination of the quantum numbers of relevance. For the even isotopes, the electronic angular momentum J and the magnetic

M_J are required. In the weak field regime, the total angular momentum F and the magnetic M_F quantum numbers are needed to identify the hyperfine sub-levels [25, 26]. However, in the strong field case, F and M_F are undefined quantum numbers therefore the set (I, J, M_I, M_J) needs to be used instead. Afterwards, the allowed transitions are set by the values of $\Delta M_{F,J}$. The latter are selected by accounting for the laser polarization with respect to the local direction of magnetic field. In this experiment, the laser beam is parallel to the magnetic field, therefore only the σ components ($\Delta M_{F,J} = \pm 1$) are allowed. The selection rule $\Delta M_I = 0$ is additionally considered whenever the strong field condition is met. These selection rules lead to 12 lines for the each even isotope, 36 for ^{129}Xe and 108 for ^{131}Xe.

The energy shift of each transition is computed as the sum of three terms: the isotopic shift, the contribution of the hyperfine structure, the contribution of the magnetic field. The values of the isotopic shifts of interest are tabulated in [32]. It is chosen to refer these shifts to ^{132}Xe since it is the most abundant isotope. The hyperfine structure term is nonzero for the odd isotopes only and it is function of the hyperfine constants A and B [25, 31, 33, 34]. The magnetic field contribution is a function of the magnetic quantum number $M_{F,J,I}$, the strength of the magnetic field and the Landé g-factor. Complete expressions are found in [31] and the required constants are provided in [28, 35].

At this stage, the complete spectrum is built by determining the relative intensity of each line. The formulation is reported in [31] for each $\Delta M_{F,J}$ component‡. These intensities require to be weighted accounting for natural abundance of each isotope [30] and hyperfine components tabulated in [36] as a function of I, ΔJ and ΔF.

Doppler broadening of each transition is addressed by applying a Gaussian profile exhibiting identical width and frequency shift to each line. Here the laser beam profile is considered as a Dirac delta function due to its bandwidth (< 1 MHz), and the natural width (5 MHz) is neglected in comparison to the Doppler broadening full width at half maximum (in the order of 1 GHz at typical kinetic temperatures) [26]. Eventually, the theoretical fluorescence profile stems from the sum of all individual Gaussian profiles.

The width of each Gaussian component is function of the ion kinetic temperature T_i, which is a free parameter in this analysis. It is worth mentioning that the broadening linked to T_i represents the spread in the axial ion velocity. As an example, Figure 5 shows

‡ The results are obtained by direct substitution of $|JM_J\rangle$ and $|FM_F\rangle$ in the equations reported in [31]. The extent to which these intensities are approximations was not explored here.

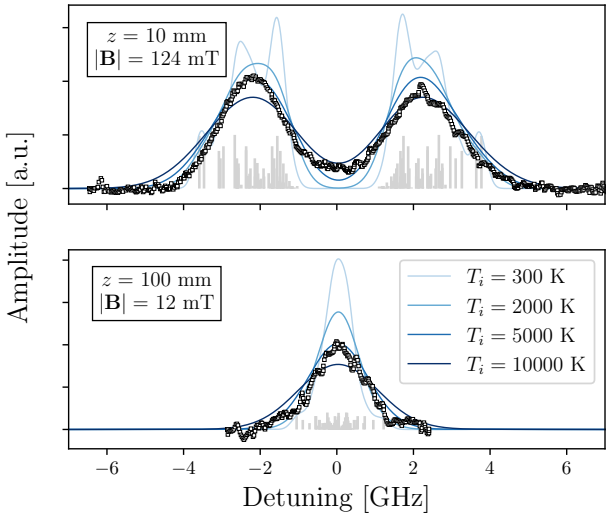

Figure 5. Comparison of experimental (squares) versus modeled (solid lines) lineshapes using arbitrary values for T_i. The experimenal data points are Doppler shifted to fit the model profiles. The bar plot images the allowed optical transitions. Thruster operation parameters are: $P_F = 200$ W, $\dot{m} = 2$ sccm, $I_c = 5$ A.

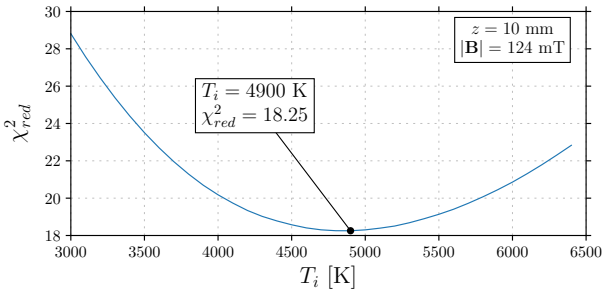

Figure 6. Instance of χ^2_{red} evolution with T_i. The highlighted point at $T_i = 4900$ K identifies the value that best fits the spectrum recorded at $z = 10$ mm, whereas T_i that minimizes $\bar{\chi}^2_{red}$ of the whole series equals 4700 K. These data are relative to the set of profiles recorded at: $P_F = 200$ W, $\dot{m} = 2$ sccm, $I_c = 5$ A.

two experimental profiles along with a few theoretical lineshapes computed using arbitrary values of T_i for the sake of comparison. In this case, one can observe a good agreement with the experimental data when $T_i \approx 5000$ K. For a more consistent determination of T_i, the algorithm relies on the computation of the reduced-χ^2 metric (χ^2_{red}), which quantifies the goodness of fit given the experimental and theoretical lineshapes. For a fixed set of thruster operating parameters, χ^2_{red} is computed for each spectrum and then averaged over all spectra giving $\bar{\chi}^2_{red}$. By that means, T_i is chosen with a resolution of 100 K as the value that outputs a value of $\bar{\chi}^2_{red}$ closer to 1. An example of how χ^2_{red} evolves as a function of T_i is

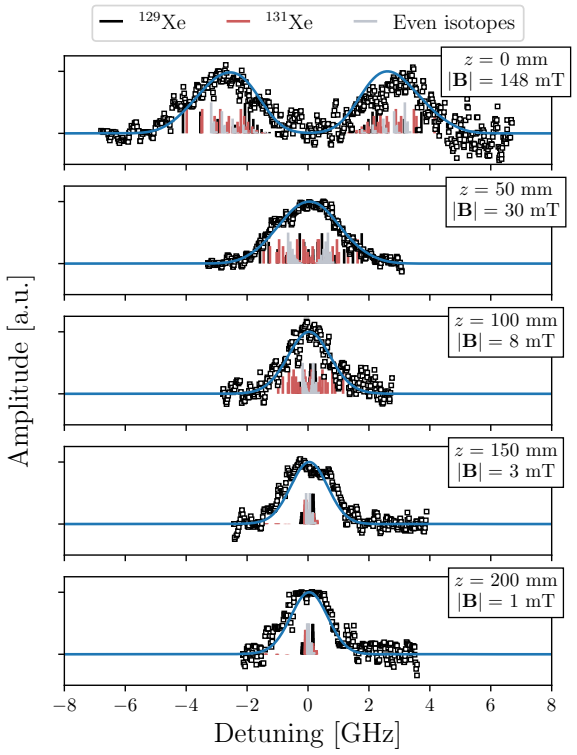

Figure 7. Experimental (squares) versus modeled (line) lineshape of Xe II. The experimental data points are Doppler shifted to fit the model profile. Thruster operation parameters are: $P_F = 200$ W, $\dot{m} = 1$ sccm, $I_c = 0$ A.

provided in Figure 6. In doing so, it is intrinsically assumed that T_i does not change throughout the plasma expansion. However simplistic, this procedure did not show the need to consider different values of T_i as the axial position z varies. In fact, it shall be shown later that the theoretical and experimental profiles are generally found to be in good agreement. A different approach would consist in computing the ion kinetic temperature that provides the best fit for each individual measured lineshape, so as to yield a function in the form of $T_i(z)$ for a fixed set of thruster operation parameters. For further completeness, an implementation of this kind has been performed within the fitting algorithm. However, as a general remark, no clear trend of T_i associated with the axial coordinate is found. Thus, a relatively small ($\lesssim 10\%$) difference in T_i along z is most probably related to concurrent uncertainties, e.g. noise level, quantum constants, robustness of the fitting algorithm, thruster stability at fixed operation parameters, departure from equilibrium. Therefore, this more general analysis suggests that the proposed use of $T_i(z) = T_i$ can be regarded as a valid approach.

As a final step, once the Doppler broadened line is

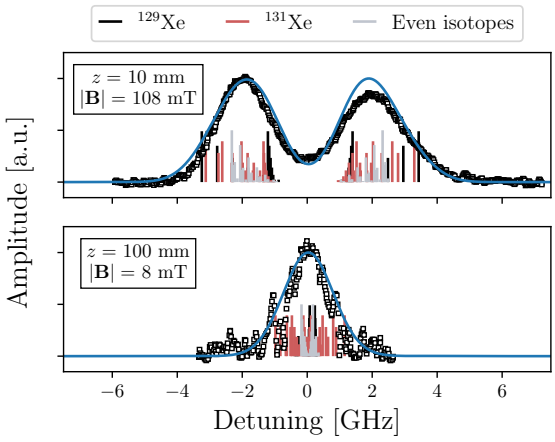

Figure 8. Experimental (squares) versus modeled (line) lineshape of Xe II. The experimental data points are Doppler shifted to fit the model profile. Thruster operation parameters are: $P_F = 200$ W, $\dot{m} = 2$ sccm, $I_c = 0$ A.

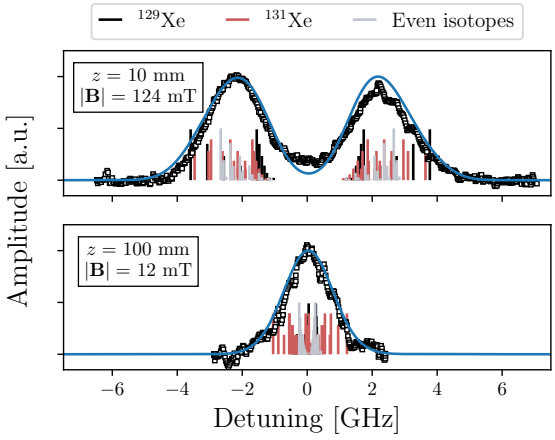

Figure 9. Experimental (squares) versus modeled (line) lineshape of Xe II. The experimental data points are Doppler shifted to fit the model profile. Thruster operation parameters are: $P_F = 200$ W, $\dot{m} = 2$ sccm, $I_c = 5$ A.

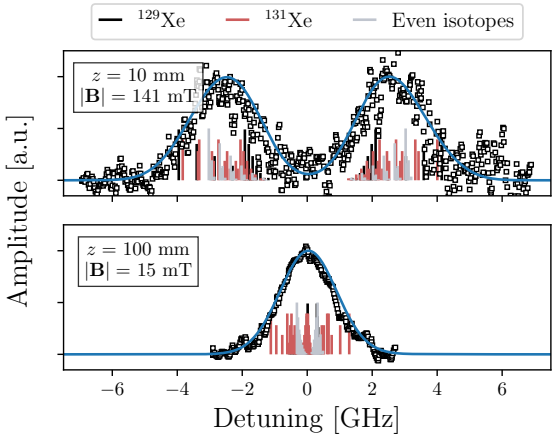

Figure 10. Experimental (squares) versus modeled (line) lineshape of Xe II. The experimental data points are Doppler shifted to fit the model profile. Thruster operation parameters are: $P_F = 200$ W, $\dot{m} = 2$ sccm, $I_c = 10$ A.

generated, the most probable ion velocity is estimated from the Doppler shift equation [23]. This shift is equal to the off-set in the frequency axis that gives the best match between the experimental and modeled lineshapes with a precision of 10 MHz (≈ 8 m s^{-1}). The error associated with the ion velocity computation results from several contributing factor, such as the uncertainty on hyperfine constants and isotopic shifts in input, the quality of the raw data, the robustness of the fitting algorithm. By exploring the full range of uncertainties of the input constants to the model (i.e. isotopic shifts and hyperfine constants) and different filtering parameters on the noisy signals, it is estimated that the typical uncertainty in the velocity value is below the absolute accuracy of the wavemeter.

Figure 7 to Figure 10 provide different instances of model outcomes compared to experimental spectra. Figure 7 reports a series of axial scans which cover a broad region spanning from the thruster exit plane up to 20 cm downstream. The model adequately predicts the fluorescence lineshape for all of these very different conditions, i.e. from strong magnetic field at $z = 0$ up to fairly negligible magnetic field at $z = 200$ mm. For this series of spectra, a kinetic temperature of 3900 K represents the best fitting value, yielding $\bar{\chi}^2_{red} \simeq 2$. Figure 8, 9 and 10 show the theoretical and experimental LIF profiles at $z = 10$ mm and $z = 100$ mm when the additional coil of the thruster is powered with 0 A, 5 A and 10 A, respectively. Also in these cases, the modeled lineshape is in close agreement with the measurements. A kinetic temperature between 4700 K and 6400 K is found to fit these data, leading to $\bar{\chi}^2_{red} \simeq 5 - 20$, see Figure 6.

It shall be pointed out that the typical T_i observed in this experiment is notably larger that what reported in previous studies concerning magnetic nozzle dynamics [24], where $T_i < 1000$ K were found. At such low plasma pressures typical of the source in analysis here, ion heating due to electron impact collisions cannot explain such high temperatures. Thermalization is rather a relevant phenomenon for other operating regimes related to VASIMR and MPD thrusters. Conversely, in this case, a large value of T_i in the axial direction, i.e. a dispersion in the axial velocity, is rationally attributed to an extended ionization region that overlaps with the acceleration region. This process then would lead to an anisotropy in the ion kinetic temperature between parallel and perpendicular directions. The same phenomenon has been often observed in Hall thrusters, where the spread in axial velocity essentially matches the spread in potential across which ions are produced and it reads up to a few tens of eV [22, 23, 37]. However, the dispersion here is noticeably lower than what is typically found in Hall thrusters due to the presence of the magnetic nozzle which enhances the axial electron conductivity, whereby significant potential drops within short distances are unrealistic. In principle, dispersion in ion velocity could also originate from thruster unstable and/or oscillatory behaviors during a laser frequency tuning scan. The occurrence of these transients was continuosly monitored by measuring the microwave reflected power and V_T and data were acquired only during steady state operation.

3.3. Velocity profiles

A parametric approach is followed in performing the present experiment. Measurements are clustered into three main blocks, each of which analyzes the effect due to the variation of a single external parameter: *i*) an electromagnet current series; *ii*) a mass flow rate series; *iii*) an input power series. Results in terms of most probable axial velocity of the ions are respectively reported in Figure 11, 12 and 13. These values are computed from the Doppler shift of the fluorescence spectra as discussed in Section 3.2.

The electromagnet current series, see Figure 11, is recorded using constant values of $P_F = 200$ W and $\dot{m} = 2$ sccm, whereas the current driven in the external electromagnet is varied between $I_c = 0, 5, 10$ A. Increasing the electromagnet current has three main effects: *i*) the magnetic field strength in the PC increases; *ii*) the ECR layer shifts downstream; *iii*) the expansion rate of the MN decreases or, in other terms, the nozzle becomes longer. It is observed that, at $z = -10$ mm, the ions are mostly directed towards the thruster backplate ($v_z \approx -500$ m s^{-1}), where they will recombine. This suggests that the peak in plasma potential is positioned between $-10 < z < 0$ mm. This result holds regardless of I_c. Most of the momentum gain occurs within 5 cm downstream the exit plane, yet at different rates depending on I_c. A higher I_c is associated with a lower acceleration, which is compatible with a lower axial variation rate of the magnetic field intensity. Farther downstream instead, any difference linked to the shape of the MN is smoothed out and every configuration leads to a nearly identical axial velocity profile. This suggests that varying I_c does not significantly affect the total plasma potential drop in this experiment. A rather constant V_T has been observed between the three working points ($\approx 70 - 80$ V), qualitatively confirming that the condition in the source were similar. However, it is expected that a non-negligible difference among the various MN shapes might be preserved in terms of plume divergence, as visually noticed in Figure 3. This aspect, though analyzed in [20], requires further investigation and experimental data.

The mass flow rate series, cf. Figure 12, is recorded using constant values of $P_F = 200$ W and $I_c = 0$ A.

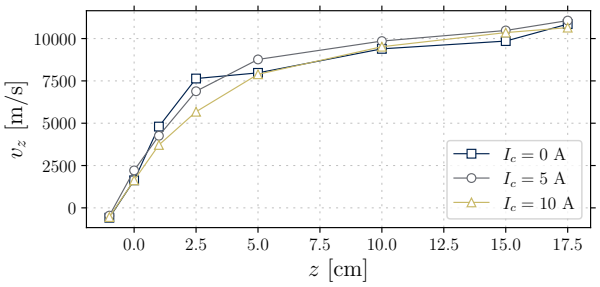

Figure 11. Most probable axial velocity profile of Xe II for different electromagnet currents. Constant thruster operation parameters are: $P_F = 200$ W, $\dot{m} = 2$ sccm.

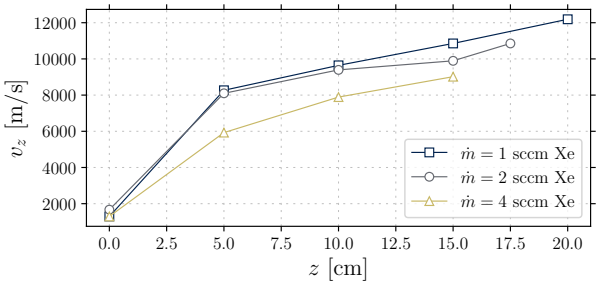

Figure 12. Most probable axial velocity profile of Xe II for different propellant mass flow rates. Constant thruster operation parameters are: $P_F = 200$ W, $I_c = 0$ A.

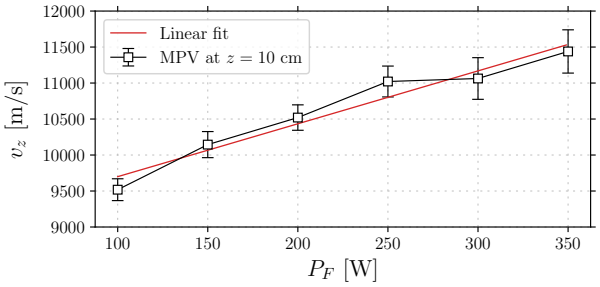

Figure 13. Most probable axial velocity of Xe II at $z = 10$ cm for different levels of input power. The error bar identifies the standard deviation given by T_i. Constant thruster operation parameters are: $\dot{m} = 2$ sccm, $I_c = 0$ A.

The farthest distance at which the ion velocity could be resolved is limited by the LIF signal-to-noise ratio. The latter is deteriorated at larger mass flow rates due to larger collision rates giving a less populated group of ions in the metastable state. In accordance with previous observations reported in the literature in terms of specific impulse [21] and ion axial velocity [12, 24], ions gain a larger momentum as the pressure of neutrals drops. This phenomenon is attributed to two effects as the mass flow rate increases: a reduced amount of deposited energy per electron and a reduced mean free path for electron-neutral and ion-neutral collisions. The first effect leads to a reduced electron temperature, hence a smaller potential drop along the expansion. On the other hand, the electron-neutral collisions contribute to electron cooling inside the source therefore lowering the internal energy available for ion acceleration through the MN, whereas ion-neutral collisions represent a drag force component which further reduces the ion kinetic energy [38].

The input power series, whose results are reported in Figure 13, is recorded at $z = 10$ cm at constant value of $\dot{m} = 2$ sccm and $I_c = 0$ A. Within the explored range of P_F, the ion axial velocity along the MN axis shows an approximately linear growth with the microwave input power, although it is expected to saturate as the thrust efficiency decays for higher powers, as shown by direct thrust measurements performed on this device [21]. As opposed to the case shown in Figure 12, increasing the power at constant $\dot{m}$ rises the available energy per electron, therefore T_e increases along with the plasma potential drop. It is noted that the value of v_z for $P_F = 200$ W measured in the power series differs by roughly 10 % from the same point shown in Figure 11 and Figure 12. This discrepancy is attributed to a slightly different condition of the thruster operation, since the two measurements are performed over different time frames. As a matter of fact, the reading of the floating potential at the source walls differs by about 15 V from one day to the next. This qualitatively indicates that the conditions in the source were slightly different and most probably a lower plasma potential drop was achieved, giving rise to a difference in the measured ion velocity.

4. Conclusion

The dynamics of xenon ions has been spatially resolved by way of laser-induced fluorescence spectroscopy along the axis of a circular waveguide electron cyclotron resonance thruster. In the near-field plume and inside the source chamber, inference of ion velocity and parallel ion temperature requires intensive lineshape modeling efforts. One must account for several broadening mechanisms, namely isotopic shift, hyperfine structure and Paschen-Back/Zeeman effect. This is especially true for ECRTs operating at relatively high frequencies which imply the need for more intense magnetic fields to meet the resonance condition.

Findings show that ions are considerably accelerated within a few centimeters downstream the exit plane, although a non-negligible amount of kinetic energy is gained in the far-field region. When the divergence of the magnetic nozzle is reduced, the accelera-

tion profile stretches out along the axis but altogether the ultimate ion velocity on-axis does not exhibit a visible dependence on the nozzle shape, in accordance with the simplest MN theories. As a general rule already observed elsewhere, a faster ion beam is attained at lower mass flow rates and higher levels of input power. Pertaining to the range explored in this experiment, it is observed that the ion velocity increases linearly with input power. Overall, the largest ion velocity recorded here reads about $12\,000\,\mathrm{m\,s^{-1}}$ at $z = 20$ cm for 200 W of input power and 1 sccm of mass flow rate. Furthermore, negative ion velocities were found in the middle of the plasma chamber at $z = -10$ mm, indicating non-negligible ion flux lost at the thruster backplate, which emphasizes that this is an important loss term in the overall thruster efficiency.

By modeling the fluorescence lineshape, it was possible to deduce the Doppler broadening width which reads about 1.5 GHz (full width at half maximum), yielding a parallel ion kinetic temperature in the order of a few thousands of K. This relative high dispersion in ion axial velocity likely results from a broad ionization region which overlaps with the acceleration region. Measurements show no evidence of ion temperature evolution along the plume expansion axis, in agreement with collisionless MN theories.

Further work must include measurements of complementary quantities of the expanding flow. Among others, it is of major relevance to investigate the neutrals velocity, the neutrals temperature and the perpendicular ion temperature. The latter two are expected to be close to the chamber walls temperature, i.e. in the order of a few hundreds of K. Ultimately, iterations on the thruster design could target the propellant injector position to reduce the amount of back-streaming ions as well as altering the overlapping acceleration-ionization regions.

Acknowledgments

This work has been supported by the PROMETEO project, funded by the Comunidad de Madrid, under Grant reference Y2018/NMT-4750 PROMETEO-CM, and it was also carried out in the frame of the Santander Chair of Excellence from the Carlos III University in Madrid granted to Dr. S. Mazouffre in 2020. Additional support came from the ESPEOS project, funded by the Agencia Estatal de Investigación (Spanish National Research Agency), under Grant number PID2019-108034RB-I00/AEI/10.13039/501100011033).

References

[1] Charles C, Boswell R, Laine R and MacLellan P 2008 *Journal of Physics D: Applied Physics* **41** 175213 URL https://doi.org/10.1088/0022-3727/41/17/175213

[2] Sheppard A J and Little J M 2020 *Plasma Sources Science and Technology* **29** 045007 URL https://doi.org/10.1088/1361-6595/ab759e

[3] Bellomo N, Magarotto M, Manente M, Trezzolani F, Mantellato R, Cappellini L, Paulon D, Selmo A, Scalzi D, Minute M, Duzzi M, Barbato A, Schiavon A, Di Fede S, Souhair N, De Carlo P, Barato F, Milza F, Toson E and Pavarin D 2021 *CEAS Space Journal* ISSN 1868-2510 URL https://doi.org/10.1007/s12567-021-00374-4

[4] Takahashi K, Charles C, Boswell R and Ando A 2013 *Journal of Physics D: Applied Physics* **46** 352001 URL https://doi.org/10.1088/0022-3727/46/35/352001

[5] Takahashi K 2019 Helicon-type radiofrequency plasma thrusters and magnetic plasma nozzles *Reviews of Modern Plasma Physics* vol 3 (Springer Singapore) ISBN 0123456789 URL https://doi.org/10.1007/s41614-019-0024-2

[6] Takahashi K 2021 *Scientific Reports* **11** 1–12 ISSN 20452322 URL https://doi.org/10.1038/s41598-021-82471-2

[7] Cannat F, Lafleur T, Jarrige J, Chabert P, Elias P Q and Packan D 2015 *Physics of Plasmas* **22** 053503 URL https://aip.scitation.org/doi/abs/10.1063/1.4920966

[8] Stix T H 1992 *Waves in plasmas* (American Institute of Physics)

[9] Bittencourt J 2004 *Fundamentals of plasma physics* (Springer, Berlin, Germany)

[10] Ahedo E and Merino M 2010 *Physics of Plasmas* **17** 073501 URL https://doi.org/10.1063/1.3442736

[11] Jarrige J, Elias P, Cannat F and Packan D 2013 Characterization of a coaxial ecr plasma thruster *44th AIAA Plasmadynamics and Lasers Conference, San Diego* URL https://doi.org/10.2514/6.2013-2628

[12] Correyero S, Jarrige J, Packan D and Ahedo E 2019 *Plasma Sources Science and Technology* **28** 095004 URL https://doi.org/10.1088/1361-6595/ab38e1

[13] Peterschmitt S and Packan D 2021 *Journal of Propulsion and Power* **37** 806–815 URL https://doi.org/10.2514/1.B38156

[14] Jahn R 2006 *Physics of Electric Propulsion* (Dover)

[15] Miller D B and Gibbons E F 1964 *AIAA Journal* **2** 35–41 ISSN 0001-1452, 1533-385X URL https://doi.org/10.2514/3.2210

[16] Kosmahl H, Miller D and Bethke G 1967 *Journal of Applied Physics* **38** 4576–4582 URL https://doi.org/10.1063/1.1709188

[17] Crimi G, Eckert A and Miller D 1967 Microwave driven magnetic plasma accelerator studies (cyclops) Tech. rep. General Electric Company, Space Sciences Laboratory, Missile and Space Division

[18] Sercel J 1993 *An experimental and theoretical study of the ECR plasma engine* Ph.D. thesis California Institute of Technology

[19] Inchingolo M R, Merino M and Navarro-Cavallé J 2021 Hybrid pic-fluid simulation of a waveguide ecr magnetic nozzle plasma thruster *Space Propulsion Conference 2020+1* 00192 (March 17-19)

[20] Inchingolo M, Navarro-Cavallé J and Merino M 2022 *Submitted to Plasma Sources Science and Technology*

[21] Inchingolo M, Navarro-Cavallé J and Merino M 2022 Direct thrust measurements of a circular waveguide electron cyclotron resonance thruster *37 th International Electric Propulsion Conference* IEPC-2022-338 (Boston, MA, June 19-23: Electric Propulsion Rocket Society)

[22] Mazouffre S, Kulaev V and Luna J P 2009 *Plasma Sources Science and Technology* **18** 034022 URL https://doi.org/10.1088/0963-0252/18/3/034022

[23] Mazouffre S 2012 *Plasma Sources Science and Technology* **22** 013001 URL

https://doi.org/10.1088/0963-0252/22/1/013001
[24] Vinci A E, Mazouffre S, Gómez V, Fajardo P and Navarro-Cavallé J 2022 *Plasma Sources Science and Technology* **31** 095007 URL https://doi.org/10.1088/1361-6595/ac8db8
[25] Pawelec E, Mazouffre S and Sadeghi N 2011 *Spectrochimica Acta Part B: Atomic Spectroscopy* **66** 470–475 ISSN 0584-8547 URL https://doi.org/10.1016/j.sab.2011.05.009
[26] Mazouffre S, Bourgeois G, Garrigues L and Pawelec E 2011 *Journal of Physics D: Applied Physics* **44** 105203 URL https://doi.org/10.1088/0022-3727/44/10/105203
[27] Lejeune A, Bourgeois G and Mazouffre S 2012 *Physics of Plasmas* **19** 073501 URL https://doi.org/10.1063/1.4731688
[28] Kramida A, Ralchenko Y, Reader J and Team N A 2020 NIST Atomic Spectra Database (ver. 5.8), [Online]. Available: https://physics.nist.gov/asd [2021, September 16]. National Institute of Standards and Technology, Gaithersburg, MD.
[29] Wachs B and Jorns B 2020 *Plasma Sources Science and Technology* **29** 045002 URL https://doi.org/10.1088/1361-6595/ab74b6
[30] Sansonetti J E and Martin W C 2005 *Journal of Physical and Chemical Reference Data* **34** 1559–2259 URL https://doi.org/10.1063/1.1800011
[31] Woodgate G K 1980 *Elementary Atomic Structure* (Oxford University Press) ISBN 0-19-851146-9
[32] Smith T, Ngom B, Linnell J and Gallimore A *Diode Laser-Induced Fluorescence of Xenon Ion Velocity Distributions* URL https://arc.aiaa.org/doi/abs/10.2514/6.2005-4406
[33] Sargsyan A, Tonoyan A, Hakhumyan G, Leroy C, Pashayan-Leroy Y and Sarkisyan D 2015 *Optics Communications* **334** 208–213 ISSN 0030-4018 URL https://doi.org/10.1016/j.optcom.2014.08.022
[34] Broström L, Kastberg A, Lidberg J and Mannervik S 1996 *Phys. Rev. A* **53**(1) 109–112 URL https://link.aps.org/doi/10.1103/PhysRevA.53.109
[35] Fuller G H 1976 *Journal of Physical and Chemical Reference Data* **5** 835–1092 URL https://doi.org/10.1063/1.555544
[36] Kopfermann H 1958 *Nuclear Moments* (*Pure and Applied Physics* vol 2) (Elsevier) URL https://doi.org/10.1016/B978-1-4832-3061-0.50001-5
[37] Szabo J J 2001 *Fully kinetic numerical modeling of a plasma thruster* Ph.D. thesis Massachusetts Institute of Technology, Dept. of Aeronautics and Astronautics URL http://hdl.handle.net/1721.1/8889
[38] Collard T A and Jorns B A 2019 *Plasma Sources Science and Technology* **28** 105019 URL https://doi.org/10.1088/1361-6595/ab2d7d